Vietnam Journal of Science and Technology
DOI: https://doi.org/10.15625/2525-2518/23429

Electrode area correction in the evaluation of DC electrical properties of ZnO-based varistors

Do Quang Tham[1,2,*], Nguyen Trung Huy[1,2], Nguyen Tuan Hung[3], Nguyen Tuan Anh[1], Nguyen Dinh Anh Son[4], Nguyen Thi Xuyen[2], Pham Thi Nam[2], Vo Thi Kieu Anh[2], Nguyen Van Trang[2], Cao Thi Hong[2], Nguyen Thi Thu Trang[2], Tran Dai Lam[2]

[1]*Graduate University of Science and Technology, VAST, 18 Hoang Quoc Viet, Nghia Do Ward, Ha Noi, Viet Nam*
[2]*Institute of Materials Science, VAST, 18 Hoang Quoc Viet, Nghia Do Ward, Ha Noi, Viet Nam*
[3]*Center for MicroElectronics and Information Technology (IMET), NACENTECH, MOST, C6 Building, Thanh Xuan Ward, Ha Noi, Viet Nam*
[4]*Hanoi University of Industry, 298 Cau Dien, Tay Tuu Ward, Ha Noi, Viet Nam*

[*]Email: *dqtham@ims.vast.vn*

Received: 10 September 2025; Accepted for publication: 15 December 2025

Abstract. This study aims to investigate the effects of electrode geometry and evaluation methods for electrode area on the electrical performance of ZnO-based varistors. A series of ZnO-based varistors was fabricated in the same composition and annealing conditions to investigate the influence of electrode geometry and electrode area evaluation methods on their electrical performance. SEM and XRD analyses of the varistors confirmed a dense microstructure with well-developed grain boundaries, with ZnO as the primary phase and modified spinel $Zn_{1.82}Cr_{0.78}Sb_{0.41}O_4$ as the main secondary phase, indicating their potential for good electrical performance as varistors and ensuring that the samples were suitable for electrical property measurements. Method 1 used the arithmetic mean, Method 2 used the geometric mean of the two electrode diameters, and Method 3 used the geometric mean with fringing correction, before calculating the area. DC electrical measurements revealed that the methods used to calculate the effective electrode diameter significantly affect the values of varistor voltages (U_{1mA}, U_{10mA}), current density (J), resistivity (ρ), and nonlinearity coefficient (α). Among these, Method 3 produced the smallest deviations in E_{1mA} and E_{10mA} and the best convergence of J–E and log(ρ)–E curves, particularly in the breakdown region. This correction also yielded the most consistent α values and minimized across-sample deviations, even in cases where electrodes had unequal sizes. These results underscore the importance of accurate area evaluation in characterizing varistor behavior.

Keywords: ZnO-based varistor, breakdown voltage, electrode area correction, DC resistivity.

Classification numbers: 2.2.2, 2.10.3, 4.1.1, 4.1.4.

1. INTRODUCTION

Zinc oxide (ZnO)-based varistors are widely used in surge protection devices due to their highly non-linear current–voltage (I–V) characteristics [1]. One important factor influencing measurement results is the electrode configuration, particularly the electrode area [2], which affects both the J–E (current density–electric field) characteristics and the derived electrical parameters. To evaluate the influence of electrode area, calculating the breakdown voltage and material resistivity provides a meaningful approach. Assuming that the breakdown voltage and resistivity of a homogeneous material remain constant under identical test conditions, any observed deviation can be attributed to geometric or contact-related factors.

Standards such as ASTM D257 and IEC 60093 provide methods for determining the volume and surface resistivity of solid insulating materials, taking into account the effective electrode area [3–7]. IEC 61643-331 focuses specifically on the specification of metal oxide varistors. This standard also deals with the electrode area as a crucial factor affecting varistor performance, but does not explicitly refer to the concept of "effective electrode area" in every clause [8]. In particular, when electrodes of different diameters are applied to the two surfaces of a disc-shaped sample, the sample under test can be modeled as a truncated cone. Thus, accurate resistance estimation must account for this conical geometry. To address this, several textbooks had assumed the uniform electric field and gave the resistance of a truncated cone, in which the model assumes axial current flow through a material of thickness h, with two electrodes of radii a and b, and uniform resistivity (ρ), and expresses the resistance (R) as shown in Eq. (1) [9]. It is noted that, the conditions a = 0 and/or b = 0 are not physically realistic.

$$R = \rho\frac{h}{\pi ab} \tag{1}$$

$$R = \rho\frac{h}{S} \tag{2}$$

Using the basic formula for the resistance of a cylinder with cross-sectional area S (Eq. (2)), the concept of effective electrode area can be applied to ZnO-based varistors. In the case of electrodes with different diameters (D_1, D_2), the varistor resembles a truncated cone, and the effective area can be expressed as $S = \pi \times D_1 \times D_2/4$, with the corresponding effective diameter given by $D = (D_1 \times D_2)^{0.5}$. In addition to geometric corrections, fringing (edge) effects also play a significant role. In three-electrode configuration (including center, unguarded and guarded electrodes), an effective diameter (D_e) is recommended applying correction using the empirical formula as Eq. (4) for circular electrode, where D_o is the actual electrode diameter and h is the sample thickness, g is the gap between the guard and center electrodes, h is the thickness of the sample, and B is a coefficient dependent on the ratio g/h (Eq. (3)).

$$B = 1 - \frac{4 \times h}{\pi \times g}\mathrm{Ln}\left\{\mathrm{Cosh}\left(\frac{\pi}{4} \times \frac{g}{h}\right)\right\} \tag{3}$$

$$D_e = D_0 + B \times g \tag{4}$$

$$B \approx 0.883 \times \frac{h}{g}, \qquad for\ \frac{g}{h} > 5 \tag{5}$$

$$D_e = D_0 + 0.883 \times h \tag{6}$$

When g/h > 5, the guard electrode has a negligible effect, and the effective diameter simplifies to $D_e = D_0 + 0.883 \times h$ (Eqs. (5) and (6)) [3]. In measuring two-electrodes systems with

electrode diameters of D_1 and D_2, the term (0.883 × h) may be added to both D_1 and D_2. Thus, the overall effective diameter D_e is then calculated as $D_e = (D_{1e} \times D_{2e})^{0.5}$.

Romano J. D. *et al.* [10] proposed an approximate formula for calculating the resistance of a truncated cone. However, their expression appears to underestimate the effective area compared to the classical formulation (Eq. (1)). Consequently, its practical application fails to deliver the expected accuracy in our case. Similarly, M. Lisowski and A. Skopec introduced a more complex expression for calculating the B-factor to correct for edge effects [4, 11]. While their formula can be applied for three-electrode systems and/or configurations with equal-sized electrodes, our experimental observations indicate that it does not yield satisfactory results when applied to truncated cone-shaped electrode configurations.

In general, many studies applied the electrode area directly from the actual silver-coated electrodes, which are commonly equal-sized, to calculate the electric properties of varistors [12–16]. However, it was theoretically noted that the fringing effect is an essential factor influencing the effective area of current conduction, particularly in configurations where the electric field is non-uniform. Ignoring this effect may lead to inaccurate evaluations of the current density and, consequently, the breakdown voltage or nonlinearity coefficient of the varistor samples. Nonetheless, this aspect has often been overlooked or insufficiently addressed in the previous studies.

In this study, the varistor material mixture was prepared in a single batch, and ZnO-based varistors were fabricated using a unified processing and sintering procedure to ensure material uniformity. Thin silver films with varying diameters were coated to the samples as electrodes. Area correction methods were also introduced, including geometric correction (for truncated cone electrode configurations) and fringing correction (for both types of electrode configurations). This controlled variation enabled a systematic investigation into how electrode area affects the resistivity, breakdown voltage, nonlinear coefficient (α), and current–voltage (I–V) characteristics of the varistor system. The experimental results were comprehensively presented and discussed. The findings of this work offer valuable insights into improving the precision and reliability of electrical measurements in varistor-based systems.

2. EXPERIMENTAL

2.1. Materials

ZnO (99,0 %) was purchased from Guangdong Guanghua SciTech company (China). Sb_2O_3, (99.99 %), Bi_2O_3, (99,0 %), Co_3O_4 (98 %), Cr_2O_3 (99.0 %), MnO_2, (99 %) purchased from Xilong Scientific company (China). Poly(vinyl alcohol) was commercial product of Duc Giang Chemical company (Viet Nam).

2.2. Preparation of ZnO-based varistor samples

Varistor samples using the same composition (molecular ratio: ZnO : Sb_2O_3 : Bi_2O_3 : MnO_2 : Co_3O_4 : Cr_2O_3 of 96.5 : 1.25 : 1.25 : 0.5 : 0.5 : 0.5 mol%) were prepared as followed. All raw materials were ball-milled with distilled water for 12 h, followed by filtration and drying at 120 °C for another 12 h. The resulting powder was mixed with 2 wt% poly(vinyl alcohol), ground in a mortar, and sieved through a 160 µm mesh. The powder was then pressed into discs (30 mm diameter, 1–2 mm thickness) at 50 MPa. The discs were preheated at 600 °C for 1 h, sintered at 1000 °C for 2 h, and slowly cooled to 100 °C over 6 h in a programmable furnace (Nabertherm

LHTC, USA). After complete cooling, the average diameter of varistor disk (D_0) was measured as 25.4 mm, or a shrinkage of about 15.3 %. Both sides of the sintered samples were polished, and silver electrodes with different diameters were applied using hollow circular masks, followed by heating at 600 °C for 10 min to form thin-film electrodes. Silver coatings were applied to the upper (D_1) and lower (D_2) surfaces of the samples, with diameter configurations of D_1:D_2 = 4:4, 10:10, 8:16, 8:8, and 3:16 mm (Table 1 and Figure 1). The creepage length (C_L) were also calculated as the average length between the outer edges of the electrodes ($C_L = 2 \times D_0 - D_1 - D_2 + h$). The labeled samples are arranged in increasing order of thickness.

Table 1. Sample labels and their electrode configurations.

Label	D4.4	S10.10	D6.16	D10.10	D8.8	D3.16
D_1 (mm)	3.96	10.53	6.12	11.08	8.51	3.19
D_2 (mm)	4.08	10.64	16.05	11.17	8.61	16.08
h (mm)	1.230	1.255	1.545	1.675	1.785	1.870
C_L (mm)	48.2	0.65	34.4	34.4	39.7	37.6

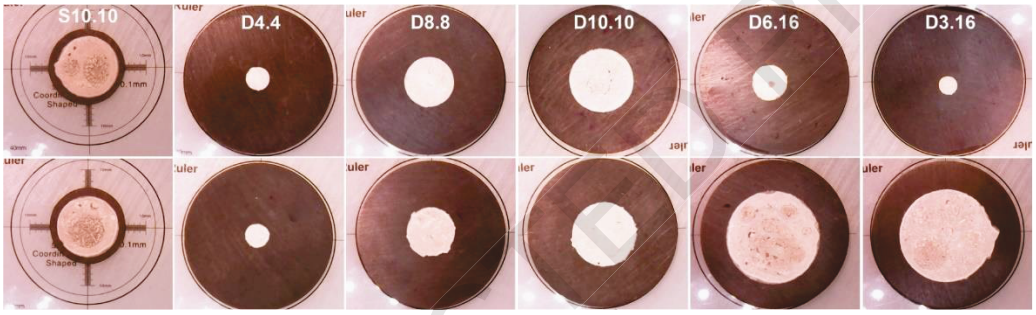

Figure 1. Different electrodes geometries coated on varistor samples.

2.3. Methods

The X-ray diffraction (XRD) patterns of the ZnO-based varistor sample was analyzed using a D8-Advance Eco Bruker diffractometer with Cu Kα radiation operated at 40 kV and 25 mA, with a wavelength of λ = 1.5406 Å.

Raman spectrum of the ZnO varistor sample was analyzed using a Raman spectrometer (Model: LabRAM HR Evolution, Horiba, Japan). The measurement was performed using an excitation laser source with a wavelength of 532 nm and a scan range from 100 to 3000 cm^{-1}.

Cross-sectional morphology of ZnO based varistor was examined using a field emission scanning electron microscopy (FESEM, JEOL 7600F, Japan). The average grain size (d) of ZnO-based varistor was determined via the linear intercept method [17]. Several lines were drawn on the SEM image, and measured their length (L [μm]) based on the scale bar of the image. With this method, the magnification coefficient (M) of the SEM image can be neglected. Next, the number of grains (N) each line were counted. The grain size (d) value was then calculated as Eq. (7), and the final value (d_a) was obtained by averaging all calculated d values.

$$d\ (\mu m) = 1.56 \times \frac{L\ (\mu m)}{N} \tag{7}$$

The volt-ampere characteristic of a varistor was conducted on a AC/DC GPT-9802A electrical safety tester (China) with a voltage ramp of 20 V/s, limit current was set at 10.90 mA, the accuracy of this current range is 0.01 mA. The GPT9802A instrument, which offers high accuracy and excellent reproducibility. For samples with similar electrode diameters, repeated measurements showed very consistent values for resistivity and breakdown voltage. Measurements were conducted in a temperature-controlled room (27 ± 2 °C, 65 % humidity) with daytime temperature variations did not exceed ± 3 °C. For samples with large electrode area, further tests were performed with higher limit current of 20 mA, the accuracy in this case is 0.1 mA. Data of voltage and current (U, I) were collected at every 150 ms from the start to the end of the measurement by using a serial port utility software (version 9.3.8, Althon Studio, China). The varistor voltages U_{1mA} and U_{10mA} are defined as the voltage at current density of 1 mA/cm^2 and 10 mA/cm^2, respectively. The U_{1mA} is also called as the reference voltage or varistor voltage [18]. It represents the voltage at which the varistor begins to conduct a significant current, specifically 1 miliampere (1mA/cm^2). Current density (J) is defined as measured current (I, mA) over effective area (S, cm^2) of the electrodes (J = I/S). The non-linear coefficient (α) is calculated via Eq. (8), where current densities J_1 = 1 mA, J_2 = 10 mA/cm^2; and E_1 and E_2 are the corresponding electric fields (E = U/h), respectively [19, 20].

$$\alpha = \frac{\log(J_2) - \log(J_1)}{\log(E_2) - \log(E_1)} = \frac{1}{\mathrm{Log}\left(E_2/E_1\right)} \tag{8}$$

$$\rho = 100 \times \frac{E}{J} \tag{9}$$

Resistivity ρ ([Ω m]) is calculated using Eq. (9), where E and J are expressed in [V mm^{-1}] and [mA cm^{-2}], respectively.

For cylindrical electrodes, the electrode diameter D can be directly and reliably used to calculate the electrode area when fringing effect is neglected. In this study, some truncated cone electrode systems were also employed, with coated electrode diameter of D_1 on the top and D_2 on the bottom of varistor sample, and $D_2 > D_1$ (as shown in Figure 1). Normally, the electrode area of an electrode geometry is often regarded as a constant value. However, this study considers different methods of area corrections depending on whether the fringing effect, the truncated electrode geometry, or both are taken into account. These corrections can lead to variations in current density and, consequently, affect the breakdown voltage results, as well as the E-J and Log[ρ]-E characteristics of the varistor. Accordingly, three different methods of applying the diameter D values are considered for each sample in the calculation. In the Method 1, D is taken as the numerical average value of the two electrode diameters (Eq. (10)). In the method 2, D is taken as the geometric mean of the two electrode diameters (Eq. (11)). In the Method 3, D is taken the value of and the geometric mean of the two effective diameters as shown in Eq. (12), where D_{1e} and D_{2e} are the fringing correction (adding 0.883×h to both D_1 and D_2), as shown in Eqs. (13) and (14), respectively. As specified in ASTM D257, the fringing-field term approaches 0.883 × h when using a two-electrode system and when the ratio g/h is larger than 5. In this study, the electrode gap (g) is calculated as half of the creepage length (C_L) listed in Table 1. This gap condition (g/h > 5) ensures that the fringing correction remains physically valid and applicable to the effective-area evaluation.

$$D = (D_1 + D_2)/2 \tag{10}$$

$$D = \sqrt{D_1 \times D_2} \tag{11}$$

$$D = \sqrt{D_{1e} \times D_{2e}} \tag{12}$$

$$D_{1e} = D_1 + 0.883 \times h \quad (13)$$

$$D_{2e} = D_2 + 0.883 \times h \quad (14)$$

3. RESULTS AND DISCUSSION

3.1. XRD spectrum and morphology of ZnO varistor

Figure 2a shows the XRD pattern of the ZnO-based varistor sample. The dominant diffraction peaks that appears at 32,0°, 34.7°, 36.5°, 47.8°, 56.8°, 63.1°, and 68.1° correspond to the hexagonal wurtzite structure of ZnO (PDF 01-075-1526), associated with the (100), (002), (101), (102), (110), (103), and (11$\bar{2}$) lattice planes, respectively. In addition to the main phase, several minor peaks attributed to secondary phases are also observed. These include Cr_2O_3, and Bi_2O_3, modified spinel phase $Zn_{1.82}Cr_{0.78}Sb_{0.41}O_4$, $Zn(Co_{1.33}Sb_{0.66})O_4$. Moreover, trace amounts of MnO_2, Mn_2O_3, Co_3O_4, and other reaction products such as $Zn_{0.982}Sb_{0.018}O$, $Zn(Co_{1.33}Sb_{0.67})O_4$ can be also detected by XRD analysis, although their peak intensities are relatively low, and not annotated in the XRD spectrum. The presence of these phases indicates that the additive oxides (such as Sb_2O_3, Bi_2O_3, Co_3O_4, MnO, and Cr_2O_3) participated in complex reactions during sintering, forming spinel-type ($Zn_7Sb_2O_{12}$) and pyrochlore-type ($Zn_2Sb_3Bi_3O_{14}$) phases [21–23], which subsequently transformed into more compositionally complex variants due to the incorporation of other dopant elements. The formation of $Zn_{1.82}Cr_{0.78}Sb_{0.41}O_4$ phase can be explained by a series of reactions (Eqs. (15) – (18)) involving ZnO, Sb_2O_3, Bi_2O_3 and Cr_2O_3, which initially produce a pyrochlore phase ($Zn_2Sb_3Bi_3O_{14}$ at about 900 °C), followed by the spinel phase ($Zn_7Sb_2O_{12}$ at higher temperature) [21], and eventually transform into the Cr-containing modified spinel product with prolonged sintering time [24, 25]. These secondary phases are typically distributed at grain boundaries and play a crucial role in controlling grain growth and enhancing the non-ohmic behavior of the varistor [26, 27].

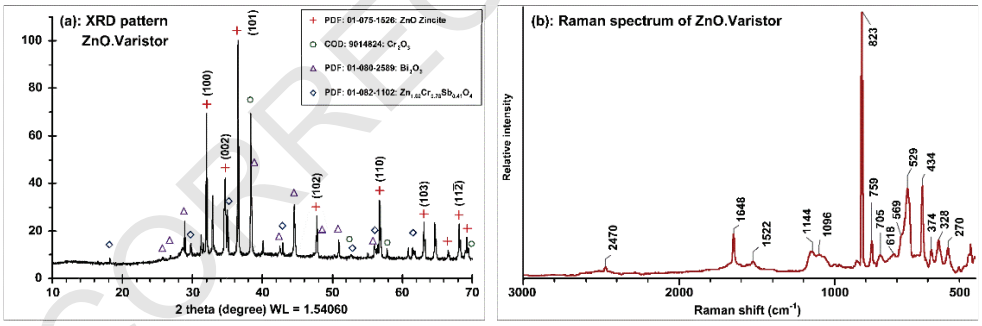

Figure 2. (a): XRD pattern of the ZnO-based varistor sample, (b): Raman spectrum of the ZnO-based varistor sample.

Unlike infrared spectroscopy, Raman spectroscopy is sensitive to low-frequency modes, allowing for the identification of the metal oxide vibrational modes (e.g, in metal oxide varistors) in the wavenumber region below 500 cm^{-1}. Figure 2b shows the Raman spectrum of the ZnO-based varistor sample. For pure ZnO crystals, the E_2(high) mode typically appears at 437 cm^{-1} [28]. In the Raman spectrum of the varistor sample, the strong and sharp peak observed at 434 cm^{-1} corresponds to the E_2(HI) mode of hexagonal ZnO, corresponding to a shift of 4 cm^{-1} [29]. This shift can be attributed to the internal stress introduced into the ZnO lattice, due to the incorporation of Bi_2O_3 and the formation of secondary phases at the grain

boundaries. The presence of the A_1(LO) mode as a shoulder at around 569 cm^{-1} suggests a certain level of defects and impurities in the ZnO grains. In previous studies [30, 31], it was reported the 823 cm^{-1} Raman peak in ZnO varistors appeared with very low intensity. In contrast, in the Raman spectrum of present sample, this peak is highly intense and prominent. Together with the strong signal at 529 cm^{-1}, this suggests a significant presence of Cr at the grain boundaries, associated with the formation of the modified spinel phase $Zn_{1.82}Cr_{0.78}Sb_{0.41}O_4$. These findings imply that the modified spinel phase has become predominant over the conventional spinel. The peak at 618 cm^{-1} corresponds to a Raman band of pyrochlore phase, its weak intensity suggests that this phase has largely transformed into a modified spinel phase. A weak Raman peak at 328 cm^{-1} is also observed, which can be ascribed to the β-Bi_2O_3 phase, possibly present as a secondary phase at the grain boundaries [30, 31].

$$ZnO + Sb_2O_3 + O_2 \rightarrow ZnSb_2O_{12} \quad (15)$$

$$3ZnSb_2O_6 + ZnO + 3Bi_2O_3 \rightarrow 2Zn_2Bi_3Sb_3O_{14} \quad (16)$$

$$2Zn_2Bi_3Sb_3O_{14} + 17ZnO \rightarrow 3Zn_7Sb_2O_{12} + 3Bi_2O_3 \quad (17)$$

$$Zn_7Sb_2O_{12} + 0.46\ ZnO + 1.17\ Cr_2O_3 \rightarrow 3Zn_{1.82}Cr_{0.78}Sb_{0.41}O_4 + 0.385\ Sb_2O_3 + 0.4075\ O_2 \quad (18)$$

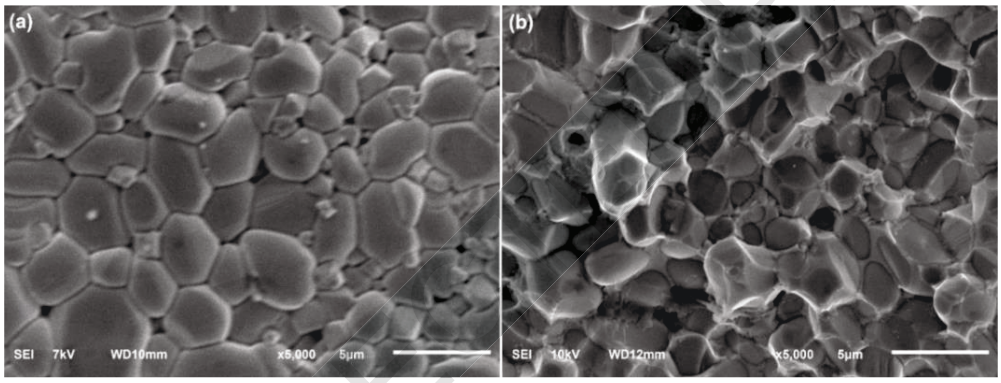

Figure 3. (a): SEM images on surface and (b) SEM images on cross-section of the varistor sample.

Figure 3 shows the SEM micrograph of the surface and fractured cross-section of the ZnO-based varistor sample. The microstructure exhibits a dense and uniform grain distribution with well-developed grain boundaries. Most grains exhibit a polyhedral morphology, typical of sintered ZnO ceramics, with clear facets indicating good crystallinity. The presence of tight grain-to-grain contact suggests effective densification during sintering. Based on the linear intercept method applied to surface and cross-section images, the average grain size (d_a) of the varistor samples was estimated to be 3.51 ± 0.5 μm and 3.86 ± 0.5 μm, respectively. No evidence of abnormal grain growth is observed in the imaged region, indicating a homogeneous microstructure favorable for varistor performance. The SEM and XRD analyses confirm that the ZnO-based varistor exhibits a dense microstructure with thin and well-defined grain boundaries [32, 33], indicating its potential for good electrical performance as a varistor.

3.2. Influence of area evaluation on the U_{nmA}

Figure 4 compares the influence of three different evaluation methods of area on the varistor voltages U_{nmA} (U_{10mA}, U_{1mA}) as functions of thickness. The methods are based on the different ways of evaluating the effective diameter of electrode systems (Eqs. 8, 9 and 10).

Since the breakdown voltage of a varistor system is proportional to number of grain boundaries or the thickness of varistor sample [34], the measurement results are considered accurate only if they at least satisfy this relationship. In the three methods presented here, both U_{10mA} and U_{1mA} exhibit a strong linear correlation with varistor thickness, confirming the expected proportionality between breakdown voltage and sample thickness. Among them, Method 1 (Figure 4a), which calculates the effective diameter as the arithmetic mean of D_1 and D_2 yields lowest correlation coefficients (R^2 = 0.9989 for U_{10mA} and R^2 = 0.993 for U_{1mA}), with a noticeable deviation observed for the D3.16 sample. In fact, when samples with equal electrode diameters (D4.4, D8.8, S10.10 and D10.10) are used as the baseline for regression, greater deviations are observed for the D3.16 and D6.16 samples. The average and deviation values of the E_{1mA} and E_{10mA} are calculated as 440.4 ± 4.9 and 480.2 ± 2.3 V mm^{-1}, respectively (for Method 1).

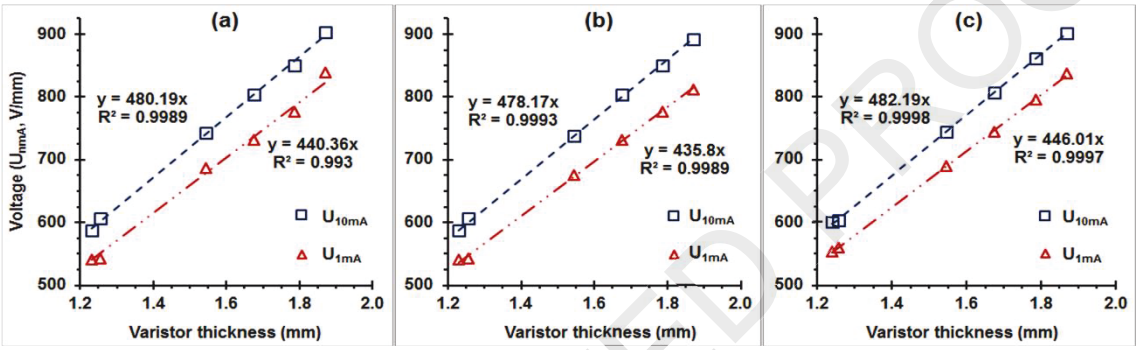

Figure 4. Variations of U_{1mA} and U_{10mA} as functions of varistor thickness, with the electrode diameter D calculated using three different methods, (a): Method 1 (D = Average[D_1, D_2]), (b): Method 2 (D= $\sqrt{D_1 \times D_2}$), and (c): Method 3 (D= $\sqrt{D_{1e} \times D_{2e}}$). (Note: The samples D4.4, S10.10, D6.16, D10.10, D8.8, and D3.16 are arranged in order of increasing thickness).

In contrast, Method 2 (Figure 4b), which uses the geometric mean of the two diameters, results in improved linearity, with high R^2 values of 0.9993 for U_{10mA} and 0.9989 for U_{1mA}, respectively. This strong agreement supports the validity of the formula in Eq. (1), in which the area (S) is calculated as $S = \pi D^2/4 = \pi D_1 \times D_2/4$. The average and deviation values of E_{1mA} and E_{10mA} for all samples are 435.8 ± 2.3 and 478.2 ± 1.8 V mm^{-1}, respectively (for Method 2).

When Method 3 is applied, the lowest deviations for the values of E_{1mA} and E_{10mA} for all samples are obtained (E_{1mA} = 445.0 ± 0.8 and 481.8 ± 1.0 V mm^{-1}, respectively (for Method 3). The highest R^2 values (0.9998 for U_{10mA} and 0.9997 for U_{1mA}) are observed in Figure 4c, indicating well improved linearity due to the inclusion of fringing effect correction ($D_{1e} = D_1 + 0.883 \times h$; $D_{2e} = D_2 + 0.883 \times h$; $S = \pi D_{1e} \times D_{2e}/4$). These findings imply that the choice of electrode diameter calculation method has a minor but measurable effect on the accuracy of the breakdown voltage–thickness correlation in ZnO varistors.

3.3. Influence of area evaluation on the coefficient α

Table 2 shows that the three electrode area evaluation methods have a significant impact on the nonlinearity coefficient (α). Method 1 gives the moderate α values (average of 26.6 ± 3), especially for varistor samples with large differences in electrode diameters (e.g D3.16 and D6.16), due to the average diameter is included with a large one, which leads to higher area, thus, higher α values. Method 2 provides lower α values (average of 24.9 ± 1.5). This supports

the application of Eq. (1) for truncated-cone geometries, even for samples with nearly equal electrode diameters, as minor differences can still affect the field distribution. However, Eq. (1) is based on the assumption of a uniform electric field, which may not be applied to samples with extremely different electrode sizes, which is outside the scope of this study. Method 3 yields the highest average α value (29.5 ± 1). This indicates that combining both the geometric mean and the fringing effect leads to a more realistic evaluation of the actual conduction area. Nevertheless, using equal and sufficiently large electrodes is still recommended to ensure field uniformity and measurement reliability. Based on Figure 4, the E_{1mA} and E_{10mA} values can be evaluated as the slopes of the regression lines. Using Eq. (8), the α values are also calculated and listed in Table 2, which shows a trend similar to the averaged α values just mentioned above. Method 1 yields an average α of 26.6 ± 3.7, Method 2 gives 24.8 ± 1.8, and Method 3 provides the highest value of 29.5 ± 1. These results further confirm the validity and advantage of Method 3 in evaluating the nonlinearity coefficient, as it not only produces the highest average α but also shows the small deviation.

Table 2. The α values of varistor samples with different electrode geometries and area estimations.

Sample label	Method 1: D = Average (D_1, D_2)		Method 2: $D = \sqrt{D_1 \times D_2}$		Method 3: $D = \sqrt{D_{1e} \times D_{2e}}$	
	Area (cm^2)	α	Area (cm^2)	α	Area (cm^2)	α
D4.4	0.127	20.8	0.127	20.8	0.205	28.0
D8.8	0.575	24.9	0.575	24.9	0.807	29.0
S10.10	0.880	28.3	0.880	28.3	1.074	30.9
D10.10	0.972	25.0	0.972	25.0	1.248	28.5
D6.16	0.965	29.2	0.771	26.1	0.943	30.1
D3.16	0.729	31.2	0.403	24.6	0.611	30.6
Average	-	26.6 ± 3.0	-	24.9 ± 1.5	-	29.5 ± 1.0
From Figure 4	-	26.6 ± 3.7	-	24.8 ± 1.8	-	29.5 ± 1.0

3.4. Influence of area estimation on the I-V curves

Figure 5 shows the effect of electrode area estimation on the J–E characteristic curves of ZnO varistors, based on three different methods for estimating the effective electrode diameter. In Figure 5, where Method 1 is applied [$D = (D_1 + D_2)/2$], the J–E curve of the D3.16 sample (in which D_2 is significantly larger than D_1) exhibits a noticeable deviation from those of samples with equal electrode diameters, such as D8.8 and S10.10. These deviations are primarily due to the fact that the arithmetic mean overestimates the effective area for samples with unequal-sized electrodes, resulting in a lower calculated current density and a shift of the J–E curve toward higher electric fields. When using Method 2, Figure 5b show that the E–J curves of varistor sample move closer together. However, a noticeable deviation is still observed for the D3.16 sample. In this case, the I-E curve of D3.16 sample shift towards lower electric field in compared with that of S10.10 sample, indicating an underestimation of effective area for the D3.16 sample. In contrast, Figure 5c demonstrates that when Method 3 is applied (combining the geometric mean with a fringing correction) all J–E curves nearly overlap, regardless of electrode geometry. This convergence of J–E curves confirms that Method 3 provides the most accurate of current density across all samples. The inclusion of fringing correction effectively compensates for edge effects, particularly in samples with large differences between top and

bottom electrode diameters. Overall, these results highlight the importance of selecting an appropriate area estimation method to ensure meaningful comparisons in the electrical characterization of ZnO varistors.

3.5. Influence of area estimation on the resistivity

Figure 6 depicts the variation of log(resistivity) of the varistor samples as a function of electric field, where three different methods for electrode diameter (or area) calculation are applied. When using Method 1, Figure 6a shows substantial differences in the resistivity of the varistor samples at all electric field levels (pre-breakdown and breakdown region), despite being fabricated from the same raw materials and under identical sintering conditions. This indicates that the applied electrode areas in the resistivity (ρ) calculation were not properly corrected. When using Method 2, Figure 6b shows that the log(ρ)–E curves are more closely grouped; however, their breakdown regions (i.e., the regions with a rapid drop in resistivity) still exhibit noticeable separation. When using Method 3, Figure 6c shows that the log(ρ)–E curves in the breakdown region are nearly overlapped, although some separation remains in the pre-breakdown region. However, in this study, particular attention is given to the breakdown behavior of the varistors. The observed differences in resistivity in the pre-breakdown region among varistor samples with different electrode geometries arise from variations in surface resistivity, which are strongly influenced by differences in creepage length resulting from the electrode configuration.

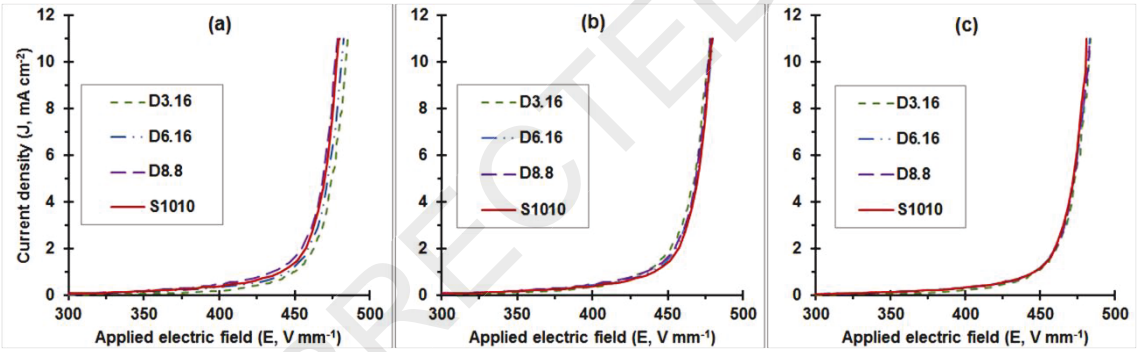

Figure 5. The J–E curves of varistor samples under three calculation methods of electrode diameter, (a) Method 1: D = Average(D_1, D_2); (b) Method 2: D = $\sqrt{D_1 \times D_2}$, and (c) Method 3: D = $\sqrt{D_{1e} \times D_{2e}}$.

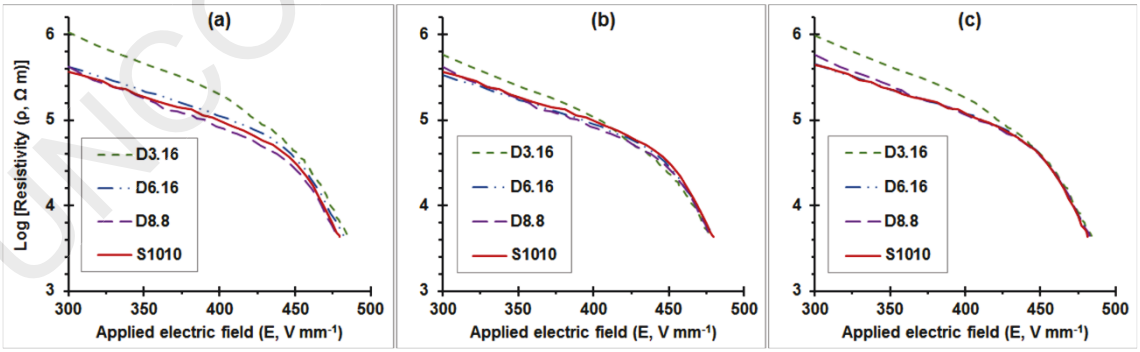

Figure 6. (a): The Log(ρ)–E curves of varistor samples under three calculation methods of electrode diameter, (a) Method 1: D = Average(D_1, D_2); (b) Method 2: D = $\sqrt{D_1 \times D_2}$, and (c) Method 3: D = $\sqrt{D_{1e} \times D_{2e}}$.

At low electric fields, both surface current and bulk current contribute to the total current through the varistor. In this region, the current values are very small, and the deviations between the E–J curves of different samples are relatively large, primarily depending on the ratio of creepage length to sample thickness. At higher electric fields, where breakdown occurs, bulk breakdown tends to dominate earlier, making the bulk current the predominant component. As a result, the influence of surface current becomes negligible. Therefore, if the effective area is properly estimated, the E–J characteristics, and likewise the resistivity curves, of varistor samples fabricated in the same batch should closely match in the breakdown region.

4. CONCLUSION

This study applied three different approaches to determine the electrode area in the calculation of DC electrical properties of ZnO-based varistors. In Method 1, the effective electrode diameter was calculated using the direct average of the two electrode diameters: $D = (D_1 + D_2)/2$. In Method 2, employed the geometric mean of the electrode diameters: $D = \sqrt{D_1 \times D_2}$. Method 3 combined the geometric mean with a fringing effect correction: $D = \sqrt{D_{1e} \times D_{2e}}$, where $D_{1e,2e} = D_{1,2} + 0.883 \times h$ (h is the thickness of varistors). The analysis revealed that the choice of method for evaluating the effective electrode diameter had a significant influence on the calculated electrical characteristics of ZnO varistor samples, particularly in the calculation of current density and resistivity. Among the three methods, the combination of geometric mean and fringing correction for effective electrode diameters (Method 3) provided the most consistent and accurate results, showing minimal deviation in both the J–E and log(ρ)–E curves across all samples, especially in the breakdown region. The analysis confirms that inaccurate evaluation of electrode area can lead to significant errors in current density and resistivity calculations, particularly for samples with unequal electrode diameters. While variations in the pre-breakdown region are mainly attributed to differences in surface resistivity influenced by creepage length, the breakdown behavior is dominated by bulk properties and thus more sensitive to the accuracy of the effective area evaluation. These findings highlight the necessity of accounting for both geometric and fringing effects when analyzing varistor samples with unequal-sized electrode configurations. Proper correction of the electrode area ensures reliable comparison of electrical properties across different sample geometries and contributes to a more accurate interpretation of varistor performance.

Acknowledgements. This research is funded from the Ministry of Science and Technology of Vietnam (MOST) for the project with grant number of ĐTĐLCN.22/23.

CRediT authorship contribution statement. Do Quang Tham: Formal analysis, Methodology, Writing – review & editing. Nguyen Trung Huy: Investigation, Writing – original draft. Nguyen Tuan Hung: Formal analysis. Nguyen Tuan Anh, Nguyen Dinh Anh Son, Nguyen Thi Xuyen, Pham Thi Nam, Vo Thi Kieu Anh, Nguyen Van Trang, Cao Thi Hong, Nguyen Thi Thu Trang: Data curation, Investigation. Tran Dai Lam: Writing – review & editing.

Declarations of competing interests. The authors declare that they have no known competing financial interests or personal relationships that could have appeared to influence the work reported in this paper.

REFERENCES

1. Ganesh K. S. – A review of zinc oxide varistors for surge arrester. In: *2018 4th international conference on electrical energy systems (ICEES)*. IEEE, (2018) 470–474. https://doi.org/10.1109/icees.2018.8443207.
2. Lee H.-G., Kim J.-G. – Volume and surface resistivity measurement of insulating materials using guard-ring terminal electrodes. Energies, **13** (2020) 2811. https://doi.org/10.3390/en13112811.
3. ASTM D257-14 – Standard test methods for DC resistance or conductance of insulating materials, ASTM International, West Conshohocken, PA, USA (2014).
4. Lisowski M., Kacprzyk R. – Changes proposed for the IEC 60093 standard concerning measurements of the volume and surface resistivities of electrical insulating materials. IEEE Trans. Dielectr. Electr. Insul., **13** (2006) 139–145. https://doi.org/10.1109/tdei.2006.1593412.
5. Küchler F., Lötscher E. R., Färber R., Franck C. M. – Polarization-depolarization current (PDC) measurements for volume and surface resistivity analysis of polymeric materials. In: *2021 IEEE conference on electrical insulation and dielectric phenomena (CEIDP)*. IEEE, (2021) 17–22. https://doi.org/10.1109/ceidp50766.2021.9705340.
6. Xu Z., Zhang Y., Zhang Y. – The influence of parameters of disk electrode with guard electrode system and sample on permittivity error caused by equivalent electrode area calculation and its correction method. Measurement, **129** (2018) 37–50. https://doi.org/10.1016/j.measurement.2018.05.048.
7. IEC 60093 – Methods of test for volume resistivity and surface resistivity of solid electrical insulating materials, International Electrotechnical Commission, Geneva, Switzerland (1980).
8. IEC 61643-311 – Components for low-voltage surge protective devices - Part 331: Performance requirements and test methods for metal oxide varistors (MOV), International Electrotechnical Commission, Geneva, Switzerland (2020).
9. Efthimiou C. J., Llewellyn R. A. – Addition laws in introductory physics. Eur. J. Phys., **26** (2005) 441–456. https://doi.org/10.1088/0143-0807/26/3/010.
10. Romano J. D., Price R. H. – The conical resistor conundrum: A potential solution. Am. J. Phys., **64** (1996) 1150–1153. https://doi.org/10.1119/1.18335.
11. Kołakowska D., Lisowski M. – The effective area of measurement electrode in volume resistivity and permittivity of solid dielectrics measurements. Meas. Autom. Monit., **61** (2015) 32–34.
12. Ashraf M. A., Bhuiyan A. H., Hakim M. A., Hossain M. T. – Microstructure and electrical properties of Ho_2O_3 doped Bi_2O_3-based ZnO varistor ceramics. Phys. B: Condens. Matter, **405** (2010) 3770–3774. https://doi.org/10.1016/j.physb.2010.05.084.
13. Lei M., Li S., Jiao X., Li J., Alim M. A. – The influence of CeO_2 on the microstructure and electrical behaviour of ZnO-Bi_2O_3-based varistors. J. Phys. D: Appl. Phys., **37** (2004) 804–812. https://doi.org/10.1088/0022-3727/37/5/024.
14. Bouchekhlal A., Boulesbaa M. – Synthesis and characterization of ZnO-based varistor ceramics: Effect of sintering temperatures. Microelectron. Int., **39** (2022) 110–120. https://doi.org/10.1108/mi-01-2022-0005.
15. Li J. -l., Chen G. -h., Yuan C. -l. – Microstructure and electrical properties of rare earth doped ZnO-based varistor ceramics. Ceram. Int., **39** (2013) 2231–2237. https://doi.org/10.1016/j.ceramint.2012.08.067.
16. Dorraj M., Zakaria A., Abdollahi Y., Hashim M., Moosavi S. – Optimization of Bi_2O_3, TiO_2, Sb_2O_3 doped ZnO-based low-voltage varistor ceramic to maximize nonlinear electrical properties. Sci. World J., **2014** (2014) 741034. https://doi.org/10.1155/2014/741034.
17. Sendi R. – Grain size and sintering temperatures effects on the mechanical properties of ZnO nanoparticle-based varistor ceramics. J. Umm Al-Qura Univ. Appl. Sci., **8** (2022) 50–56. https://doi.org/10.1007/s43994-022-00002-9.
18. Litzbarski L. S., Olesz M., Wojtas S., Winiarski M. J., Klimczuk T., Głowiński H., Andrzejewski B. – Quality assessment of low voltage surge arresters. IEEE Access, **10** (2022) 129313–129321. https://doi.org/10.1109/access.2022.3226401.

19. He J. – Metal oxide varistors: From microstructure to macro-characteristics, John Wiley & Sons, Germany (2019). https://doi.org/10.1002/9783527684038.
20. Fan J. W., Zhao H. J., Zhang X. L. – The electrical properties and impedance analysis of ZnO varistors doped with different Cu_2O contents. Appl. Mech. Mater., **681** (2014) 173–176. https://doi.org/10.4028/www.scientific.net/amm.681.173.
21. Lin W., Xu Z., Wang Z., Yang J., Zhu C., Chu R. – Influence of $Bi_3Zn_2Sb_3O_{14}$ pre-synthesis phase on electrical properties of the ZnO-Bi_2O_3-based varistor ceramics. J. Alloys Compd., **834** (2020) 155070. https://doi.org/10.1016/j.jallcom.2020.155070.
22. Liu W.-F., Zhang L., Kong F.-Y., Wu K.-N., Li S.-T., Li J.-Y. – Enhanced voltage gradient and energy absorption capability in ZnO varistor ceramics by using nano-sized ZnO powders. J. Alloys Compd., **828** (2020) 154252. https://doi.org/10.1016/j.jallcom.2020.154252.
23. Branković Z., Branković G., Poleti D., Varela J. A. – Structural and electrical properties of ZnO varistors containing different spinel phases. Ceram. Int., **27** (2001) 115–122. https://doi.org/10.1016/s0272-8842(00)00051-1.
24. Chen B.-H., Wang B.-W., Gao P.-Z., Zhang P., Chen H.-H. – Effects of raw particle size and annealing on microstructure, electrical and mechanical behaviors of ZnO-based varistors. J. Alloys Compd., **872** (2021) 159638. https://doi.org/10.1016/j.jallcom.2021.159638.
25. Hung N. T., Quang N. D., Bernik S. – Electrical and microstructural characteristics of ZnO-Bi_2O_3-based varistors doped with rare-earth oxides. J. Mater. Res., **16** (2011) 2817–2823. https://doi.org/10.1557/jmr.2001.0388.
26. Zhang L., Gao J., Liu W., Guo Q., Li S., Li J. – Simultaneously enhanced electrical stability and nonlinearity in ZnO varistor ceramics: Role of Si-stabilized δ-Bi_2O_3 phase. J. Eur. Ceram. Soc., **41** (2021) 2641–2647. https://doi.org/10.1016/j.jeurceramsoc.2020.12.008.
27. Zheng Y., Fujimoto M., Sato Y., Yoshikado S. – Effects of addition of chromium and/or nickel oxides on the electrical characteristics of yttrium oxide-doped high-voltage zinc oxide varistors. J. Eur. Ceram. Soc., **41** (2021) 4841–4849. https://doi.org/10.1016/j.jeurceramsoc.2021.03.042.
28. Klingshirn C. F., Meyer B. K., Waag A., Hoffmann A., Geurts J. – Zinc oxide: From fundamental properties towards novel applications, Springer, Berlin, Heidelberg (2010). https://doi.org/10.1007/978-3-642-10577-7.
29. Alharthi H., Sendi R., Mohammed Z., Althagafi T. – Investigation the effect of particle size and annealing on the performance of nano/micro sized ZnO-based varistors. IOP Conf. Ser.: Mater. Sci. Eng., **1269** (2022) 012008. https://doi.org/10.1088/1757-899x/1269/1/012008.
30. Huang Y., Liu M., Li Z., Zeng Y., Liu S. – Raman spectroscopy study of ZnO-based ceramic films fabricated by novel sol-gel process. Mater. Sci. Eng. B, **97** (2003) 111–116. https://doi.org/10.1016/s0921-5107(02)00396-3.
31. Tian T., Zheng L., Podlogar M., Zeng H., Bernik S., Xu K., Ruan X., Shi X., others – Novel ultrahigh-performance ZnO-based varistor ceramics. ACS Appl. Mater. Interfaces, **13** (2021) 35924–35929. https://doi.org/10.1021/acsami.1c07735.
32. Hassan M., Hussain M., Ali M., Ali S. A. – Influence of processing parameters on microstructure and electrical properties of ZnO-based varistor ceramics. Discov. Electron., **2** (2025). https://doi.org/10.1007/s44291-025-00062-1.
33. Diwald O. – Zinc oxide nanoparticles for varistors. In: Diwald O., Berger T., eds. *Metal Oxide Nanoparticles*. Wiley, (2021) 783–807. https://doi.org/10.1002/9781119436782.ch23.
34. Pillai S. C., Kelly J. M., Ramesh R., McCormack D. E. – Advances in the synthesis of ZnO nanomaterials for varistor devices. J. Mater. Chem. C, **1** (2013) 3268–3281. https://doi.org/10.1039/c3tc00575e.